

Imaging of retina cellular and subcellular structures using ptychographic hard X-ray tomography.

Panneels V.¹, Diaz A.², Imsand C.³, Guizar-Sicairos M.², Müller E.⁴, Bittermann AG.⁵, Ishikawa T.^{1,7}, Menzel A.², Kaech A.⁶, Holler M.², Grimm C.³, Schertler G.^{1,7}

¹ Division of Biology and Chemistry, Laboratory for Biomolecular Research, Paul Scherrer Institute, 5232 Villigen, Switzerland

² Division of Photon Science, Laboratory for Macromolecules and Bioimaging, Paul Scherrer Institute, 5232 Villigen, Switzerland

³ Lab for Retinal Cell Biology, Department of Ophthalmology, University Hospital Zurich, University of Zurich, Switzerland

⁴ Division of Biology and Chemistry, Laboratory for nanoscale Biology, Paul Scherrer Institute, 5232 Villigen, Switzerland

⁵ ScopeM, Scientific Center for Optical and Electron Microscopy, ETH Zürich, 8093 Zurich, Switzerland

⁶ Center for Microscopy and Image Analysis, University of Zurich, Zurich, Switzerland

⁷ Department of Biology, ETH Zurich, Zürich, Switzerland.

ABSTRACT : Ptychographic hard X-ray computed tomography (PXCT) is a recent method allowing imaging with quantitative electron-density contrast. Here, we imaged without sectioning, cellular and subcellular structures of a wild-type mouse retina, including axons and synapses with complete isotropic 3D information over tens of microns at cryogenic temperature. Comparison with tomograms of degenerative retina from a mouse model of retinitis pigmentosa illustrates the potential of this method for analysing disease processes like neurodegeneration at sub-200 nm resolution.

As a non-destructive imaging method, PXCT is very suitable for correlative imaging. Within the photoreceptor plexiform layer, we identified somatic synapses and used a small region inside the X-ray-imaged pillar for further high-resolution focused ion beam / scanning electron microscope (FIB/SEM) tomography. The subcellular structures of synapses obtained with the X-ray technique matched the EM data demonstrating that PXCT is a powerful scanning method for tissue volumes of more than 60 cells and sensitive enough for identification and statistical analysis of regions as small as 200 nm, remaining available for further structural and biochemical investigations.

This document is the accepted manuscript version of the following article:
Panneels, V., Diaz, A., Imsand, C., Guizar-Sicairos, M., Müller, E., Bittermann, A. G., ...
Schertler, G. (2021). Imaging of retina cellular and subcellular structures using
ptychographic hard X-ray tomography. *Journal of Cell Science*, 134(19), jcs258561.
<https://doi.org/10.1242/jcs.258561>

INTRO:

The sensory input for vision is located in the retina, which is part of the central nervous system. The retina contains all known photoreceptors required for vision, the majority of non-visual photoreceptors as well as a complex network of neurons and specialized cells for signal transmission and computing. It is one of the most studied and most imaged neural tissues. These studies contribute to major advancements in our understanding of intricated neuronal networks (Wassle, 2004), for example on the visual perception of motion (Behnia et al, 2014; Wernet and Desplan, 2014) and direction selectivity (Yonehara et al, 2016). A variety of imaging techniques have been a key to understanding the process of vision, and its pathological counterpart, at different tissue organisation levels, intercellular and subcellular, which are orderly organised in consecutive cells layers. The retina, mainly made of photoreceptor cells, bipolar cells and retinal ganglion cells, is classically subdivided into 7 sublayers called outer segment (OS), inner segment (IS), outer nuclear layer (ONL), outer plexiform layer (OPL), inner nuclear layer (INL), inner plexiform layer (IPL), and ganglion cells (GC) (Wassle, 2004) (**Fig. 1**). Electron microscopy (EM) has earlier enabled to get an overall 3D impression of the neural cells interconnecting along a layer using freeze-fracture scanning electron microscopy (Wassle, 2004). However, EM is most efficient for analysing subcellular structures at highest resolution, like the outer segment disks of photoreceptors generated at the cilium (Anderson and Fisher, 1975) and the sophisticated multisynapses complexes in triad or tetrad organisation at the photoreceptor ends (Prokop and Meinertzhagen, 2006). Most neurobiology studies with 3D-imaging use targeted fluorescent labelling of subcellular domains, lacking overall information of the unstained cell population. A challenging 3D mapping of the neuronal network of the mouse IPL using serial block-face EM (Helmstaedter et al, 2013) allowed to image 950 neurons in a cubic volume of 100 μm side length and established a procedure for the classification, localisation and connectivity of the neurons. However, this method involves sectioning of the sample, thereby destroying the sample and preventing further investigations.

The need for non-destructive imaging of large volumes of tissue in three dimensions, which allows for identification of regions of interest for further study, using for example correlative microscopy or proteomic/genomic analyses, drove the development of new imaging techniques (Karreman et al, 2017). Such a method is also highly desirable in imaging retina tissue, for analysing the neurons circuitry and the neural fine structure in healthy and pathological tissues. X-Ray imaging of biological structures is highly complementary in terms of sample size and spatial resolution to other imaging techniques such as electron microscopy and light microscopy. Due to the excellent penetration behaviour of X-rays into matter, thicker samples can be imaged, albeit with limited resolution (Du and Jacobsen, 2018). Soft X-ray full field microscopy can be used to image entire cells of up to about 10 μm with a resolution allowing the visualization of subcellular structures with great detail (Foglia et al, 2019; Guo and Larabell, 2019). Hard X-ray beams, having energies above 2 keV, are needed for imaging thicker biological samples up to several hundreds of micrometres (Krenkel et al, 2015). Phase contrast modalities, such as propagation-based methods (Kosior et al, 2012; Krenkel et al, 2015; Topperwien et al, 2018; Massimi et al, 2019; Kuan et al, 2020), need to be used due to the poor absorption contrast of organic matter in water at these energies. A method using hard X-ray ptychographic nanotomography, also called ptychographic X-ray computed tomography (PXCT) (Dierolf et al, 2010), has recently been used to image a 10 μm -thick piece of a computer microprocessor at a resolution down to 15 nm in 3D (Holler et al, 2017a). PXCT has also

been successfully used for biological samples, first with the imaging of resin-embedded, stained plant tissue (Guizar-Sicairos et al, 2011) and for imaging frozen cells, revealing subcellular structures in 3D (Diaz et al, 2015). The development of specific instrumentation with a cryogenic sample holder (Chen et al, 2014; Holler et al, 2018) and high-accuracy sample positioning has provided tomograms of chemically-fixed frozen-hydrated cells (Deng et al, 2018) and chemically-fixed frozen-hydrated brain tissue of about $20 \times 70 \times 70 \mu\text{m}^3$ with a resolution of about 120 nm (Shahmoradian et al, 2017; Tran et al, 2020).

Here, we present 3D imaging with PXCT of neuronal connections in the retina outer layer from wild-type mouse and VPP transgenic mouse (Naash et al, 1993), a model for retinitis pigmentosa (RP) characterized by progressive photoreceptor degeneration. A comparison of the imaging using PXCT and FIB/SEM tomography shows the excellent complementarity of both techniques.

RESULTS:

A retina preparation protocol for electron microscopy, compatible with X-ray imaging.

A retina from wild-type or retinitis pigmentosa mouse model was aldehyde-fixed, osmium-stained and plastified (**Fig. 1A**, lower inset) as described for electron transmission microscopy in (Heynen et al, 2013). A pillar of about 25 μm diameter and 50 μm height was milled using FIB/SEM, in the OPL (**Fig. 1A**, left inset) containing the plexus of terminal neuronal connections formed at the interface of the outer (photoreceptor cells) and inner (bipolar cells) retina layers. The region of interest for milling could be easily identified after SEM imaging of the retina surface, due to the rough surface of the proximal ONL (**Fig. 1A**, right inset) made of photoreceptor nuclei. The resulting pillar was placed in the centre of a gold-coated pin (Holler et al, 2017b) for X-ray imaging (**Fig 1B**). The quality of the sample was verified by scanning electron microscopy (SEM) after removing the protective carbon top-layer of the pillar (**Fig. 1B**, inset). For an adaptation of this technique to frozen-hydrated samples, see (Shahmoradian et al, 2017).

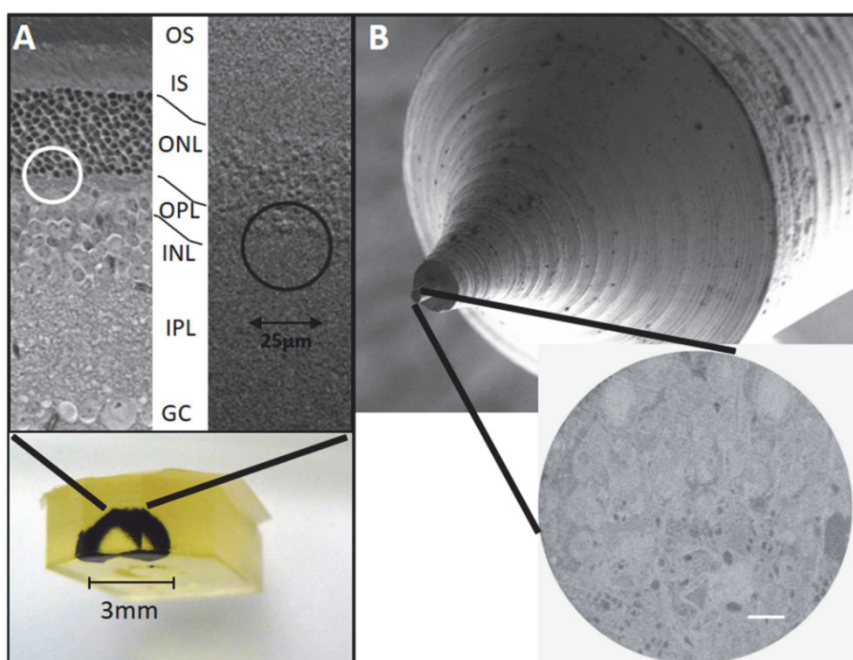


Fig.1: Retina pillar preparation for X-ray imaging. **(A)** Retina from wild-type mouse fixed with glutaraldehyde, stained with osmium, dehydrated in ethanol and embedded into Epon™ resin (lower part). A widefield light microscopy picture of a 50 nm-thick microtome section (upper left inset) shows the multiple layers of the retina: OS: outer segment, IS: inner segment, ONL: outer nuclear layer, OPL: outer plexiform layer (region of interest, white circle), INL: inner nuclear layer, IPL: inner plexiform layer, GC: ganglion cells. The corresponding region of interest was defined (black circle) by SEM imaging of the surface of the retina, right before milling (upper right inset). **(B)** Cylindrical retina pillar of about 25 μm -diameter fixed at the center of an OMNY pin (upper picture) for PXCT measurements (Holler et al, 2018; Holler et al, 2017b). The lower inset shows a SEM picture of the pillar surface, rich in cellular structures, obtained with an energy selective backscatter (ESB) electron detector. The scale bar is 3 μm .

PXCT 3D imaging of retina tissue, from cells to organelles.

The retina pillar from wild-type mouse, milled out of the OPL and slightly overlapping the ONL in order to have some rod nuclei was measured over a height of 20 μm . The reconstructed tomogram shows the overall organisation of the photoreceptor cells plexus in 3D at an isotropic half-period resolution of about 200 nm (**Fig. 2A**, **Fig. S1** and **movie 1**). The reconstructed tomogram contains about 60 photoreceptor cells nuclei.

Transversal orthoslice views across the layers (**Fig. 2B-C**) of the reconstructed tomogram show the nuclei of the ONL with the characteristic high-density chromatin ("ch"), the photoreceptors synapses ("sy") and axons ("ax"), which can be traced efficiently using a 3D viewer and analysis software. **Fig. 2D** shows a 3D segmentation of a nucleus (magenta) and the path of the photoreceptor cells axons (in green) with a diameter of about 500 nm, crossing the ONL and reaching the OPL. **Fig. 2E-G** show a zoom on several axon synaptic ends, with the typical large mitochondria "m" close to the active high electron-dense zone (labeled "az" for "active zone"). A longitudinal cut along the OPL of the retina reveals the synapses (**Fig. 2H**) populated by high electron density regions (inset) being most likely synaptic clefts ("az"). This view also demonstrates the circularity of the synapses (**Fig. 2H**).

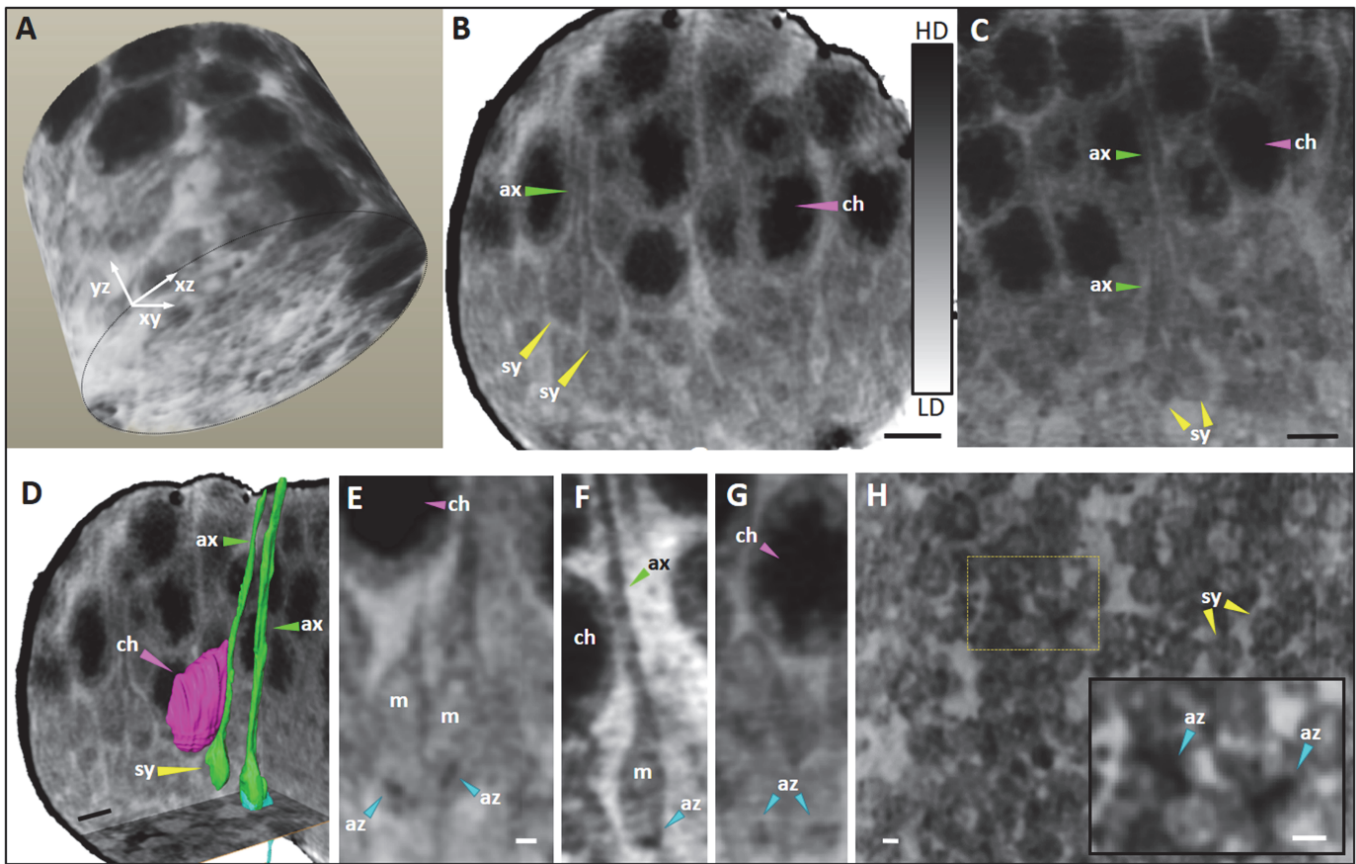


Fig.2: 3D imaging of connecting photoreceptor cells in the outer plexiform layer of a wild-type mouse measured by PXCT. (A) 3D render of the imaged tissue from the reconstructed tomogram. (B-H). Several representative sections through the reconstructed tomogram: (B-C). Transverse cross section of the retina pillar tomogram shows nuclei packed with dense chromatin ("ch" (magenta arrows)) from the outer nuclei layer (ONL) and shows axonal projections ("ax" (green arrows)) and synaptic ends ("sy" (yellow arrows)) from the outer plexiform layer (OPL) (**Movie 1**). The grayscale in panel B ranges from black representing the highest electron density (n_e) (HD, $0.45 \text{ e}/\text{\AA}^3$) to white, the lowest electron density (LD, $0.35 \text{ e}/\text{\AA}^3$) in the images. (D). 3D manual segmentation of two axons (green) and one nucleus (magenta). (E-G). A zoom on a few synapses with their characteristic large mitochondria (m) allows the identification of the smallest structures currently resolved with this method and with this type of sample: the active zone ("az" (blue arrows)) containing the ribbon (black, high electron density structure). (H). Orthoslice showing a longitudinal cross section into the OPL shows the synapses ("sy" (yellow)) and some ribbons. The ribbons of two active zones ("az" (blue arrows)) are magnified from the yellow window into the inset. Black scale bars: 3 μm (B-D). White scale bars: 500 nm (E, H).

PXCT of retina with neurodegenerative disease.

The OPL of the VPP mouse, a model for autosomal dominant RP (Naash et al, 1993; Ding and Naash, 2006) was investigated (**Fig. 3B and D**) in order to compare the tissue with the structure of the wild-type mouse (**Fig. 3A and C**) and assess whether the method is suitable for analysing biopsies from retina with degeneration. Light microscopy images (upper panels) show in the RP mouse retina the well-known loss of photoreceptors (Naash et al, 1996; Samardzija et al, 2006b) resulting in the deterioration of the rod outer segments ("OS") and progressive thinning of the ONL (**Fig. 3B**). At this developmental stage of the disease, the OPL does not seem to be dramatically affected when

observed using a classical low resolution-histology method (**Fig. 3B**). However, a closer look at the RP mouse OPL using PXCT reveals very pronounced degeneration processes compared to the wild-type at the same age and the layer does no longer display the rod synaptic ends ("sy"), called spherules, and axons ("ax") (**Fig. 3D**) (wild-type: **Movie 1** and RP-mouse: **Movie 2**). Wide-spread fibrosis can be seen in the 3D volume of the OPL, as well as bipolar cells bodies, vascularisation and synapse remnants (**Movie 2**).

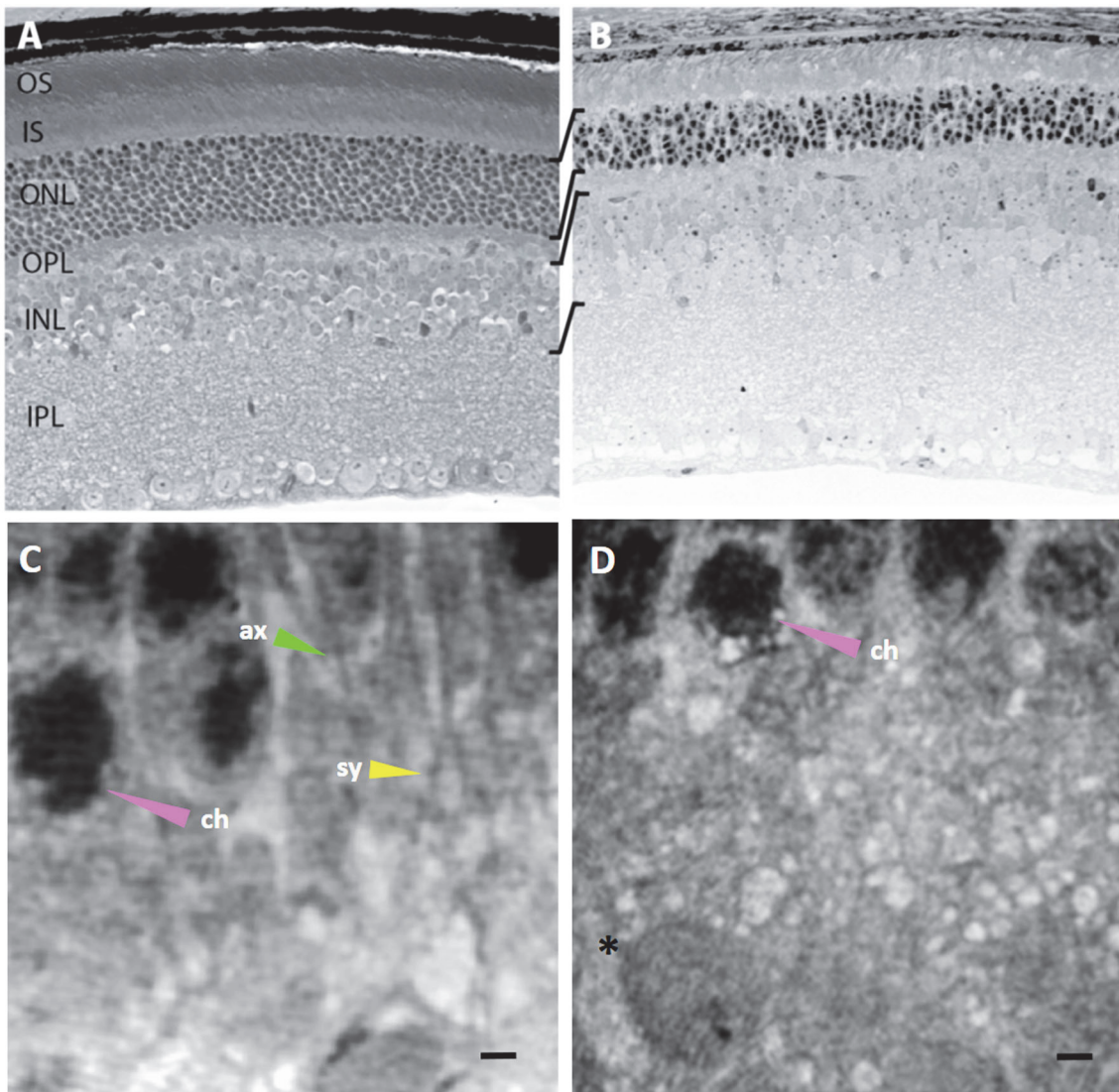


Fig.3: PXCT of the outer plexiform layer of a *retinitis pigmentosa* (RP) mouse disease model compared to wild-type. Light microscopy overview of the wild-type mouse retina (**A**) and RP-model (**B**) [for abbreviations for the different layers please see Fig.1A]. (**C-D**): 25 μm wide pillars from the respective resin-embedded samples milled from the ONL-OPL layers were imaged with PXCT. A representative section (**C**) of the tomogram from wild-type (**Movie 1**) displays the usual features, photoreceptor cell nuclei ("ch", chromatin), axons ("ax") and synaptic ends ("sy"), that are absent in the tomogram from RP retina (**D**). No identifiable axons and synaptic ends (**Movie 2**) can be seen along the RP-tomogram but a bipolar cell body (*) can be recognized down left. Scale bars are 1 μm .

The ribbon synapses: comparison of 3D imaging with electron- and hard X-ray microscopy.

The analysis of the PXCT tomograms from the wild-type retina, revealed a majority of photoreceptor synapses (**Fig. 4A**, "sy"), with the strongest electron density at the synaptic ribbon ("sr"), dense assembly of proteins and membranes of several hundreds of nanometers (Migdale et al, 2003), that were actually the smallest structures which we could observe. Besides the usual subcellular structures of photoreceptor cells, a particular feature displayed strong electron density in the bodies of a few cells located at the ONL/OPL interface. They harbor a synapse directly in the soma ("ssy") (**Fig. 4C, Fig. S2, Movie 1** (overall tomogram) **and 3** (subvolume of the tomogram, single cell)), and are easily recognized by the strong electron-dense ribbon and hilus ("h"). The hilus (Migdale et al, 2003) or hilum is a complex at the plasmic membrane region of the synaptic end, forming a common opening for the neurites to connect to the synapse.

As PXCT operates without sectioning, the integrity of the sample was preserved and further analysis like imaging at higher resolution with another technique was possible (**Flowchart Fig. S4**). Although electron microscopy usually requires multiple staining compared to the single staining used here, FIB/SEM tomography at the region of interest displayed enough contrast to see the photoreceptors nuclei, axons and synaptic ends as well as the synaptic ribbon (**Fig. 4B, Movie 4**). In some cells, preferentially at the ONL/OPL interface we could also identify in the soma, ribbon synapses like we observed with PXCT. A somatic synapse was selected (**Fig. 4D, Movie 5**) and segmented (**Fig. S3**). Ribbon synapses have already been demonstrated in the soma of cochlear afferent mechano-sensory hair cells (Wichmann and Moser, 2015), connecting to the auditory nerve fibers (Goutman et al, 2015) and also in rod cells where they seem to be increased in the Down syndrome (Li et al, 2015). The FIB/SEM tomogram shows that the synaptic ribbon of the cell body is also associated with a large mitochondria (**Fig. 4D**, "m"), a classical feature of rod synaptic ends, and flanked with vesicles distributed in proximity to the presynaptic membrane. A bunch of dendritic vesicles of about 30 nm trapped at a height between the ribbon and the hilus suggests functionality of this synapse (see yellow arrow in enlarged figure **Fig. S3F**).

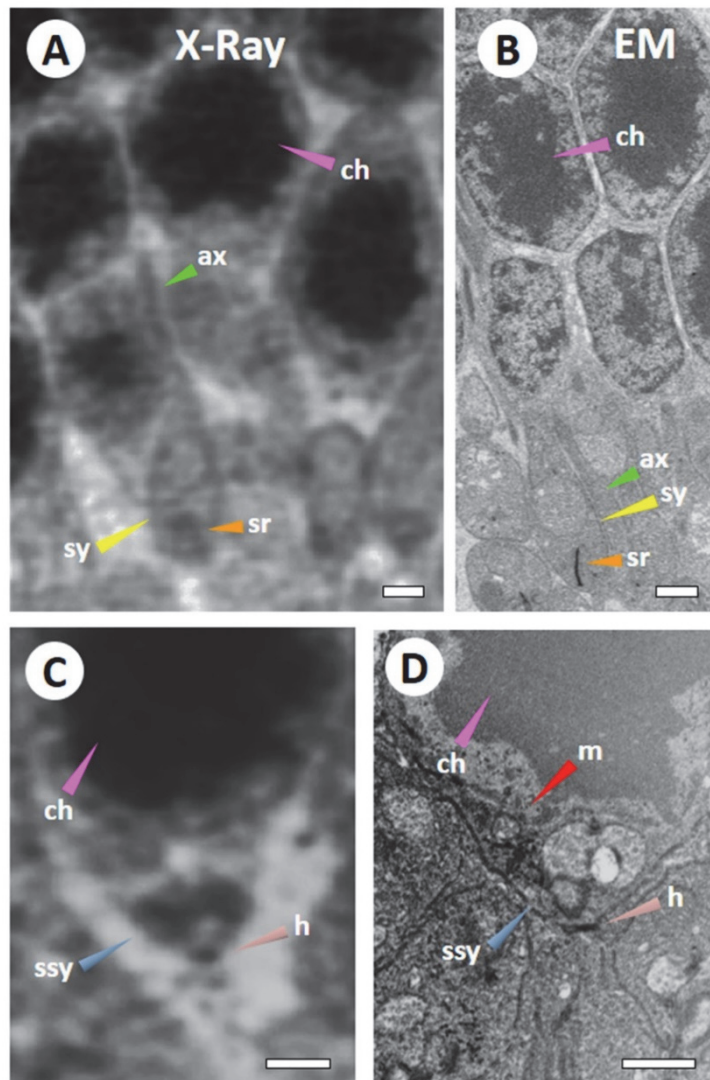


Fig.4: Comparison of the outer plexiform and nuclei layers imaged by PXCT (A and C) and FIB/SEM (B and D) on wild-type mouse

retina. A resin-embedded wild-type retina was imaged by PXCT (A) followed by FIB/SEM tomography on a similar area in the same specimen that had been used for X-ray tomography (B)(Movie 4, flowchart Fig. S4), revealing the nuclei ("ch"), axons ("ax") and typical synaptic ends ("sy") with the synaptic ribbon ("sr", orange arrows). **C-D)** Several detailed 3D features surrounding the chromatin in some neural cell bodies could be identified for both imaging methods. For example, a few somatic synapses ("ssy", blue arrow) were found in the large PXCT measurement (C), and those structures were then screened and imaged at the ONL/OPL interface of a selected smaller sample thickness (20 times thinner) of a resin-embedded retina block (**Fig. 4D, Movie 5, flowchart in Fig. S4**) at high resolution by FIB/SEM tomography. See the somatic synapse ("ssy") sitting on its hilus ("h", salmon arrows) and flanked by a large mitochondria ("m", red arrow) in (D). Scale bars are 1 μ m.

DISCUSSION:

Hard X-ray ptychographic imaging in retina physiology and pathology.

Cryo-PXCT is emerging as a powerful 3D scanning technique in biology and, allows imaging from single cells (Diaz et al, 2015) to dozens of cells while maintaining the integrity of the sample (Shahmoradian et al, 2017). Here, imaging a plastic-embedded retina pillar (25 µm diameter and 20 µm height) using PXCT, we achieve a half-period spatial resolution of about 200 nm, limited mostly by the small difference of density contrast between organelles and water with the available coherent X-ray flux. This resolution was sufficient to see large organelles and other intracellular structures like synaptic ribbons with a length of a few hundred nanometres. With its good depth of field (**Table 1**), PXCT allowed to image about 60 neuron cell nuclei, interlaced with axons traced with their synaptic ends until the plexiform layer.

The retina of a transgenic mouse, model of retinitis pigmentosa (RP), has been analysed by PXCT in the same region of interest and compared with wild-type retina. The tomograms obtained in this study demonstrate that PXCT is a highly suitable method for comparative studies on neurodegenerative disease evolution in tissues. Comparing retina of wild-type with retina of RP, a clear degeneration of the tissue is observed in 3D with a drastic reduction of synaptic ends of photoreceptor cells.

The PXCT method presented here is an excellent bridge between a low-resolution method that non-destructively scans large tissue volumes, i.e. *in vivo* hard X-ray microtomographic imaging at micrometer isotropic resolution (Walker et al, 2014), and the high-resolution imaging of thin samples, using SEM. PXCT does not require serial sectioning, thus allowing subsequent usage (Karreman et al, 2017), like the FIB/SEM tomography performed in this study. Therefore, correlative applications like high-resolution imaging or biochemical methods such as proteomics, direct *in situ* mass spectrometry analysis, and others, will be used in the future for tissue biology of complex structures in physiology and pathology disciplines, after PXCT scanning.

Hard X-ray- and electron microscopy complementarity in resolution and volume.

Conventional EM and PXCT are complementary in the resolution and accessibility of specimen volume (**Table 1**). PXCT achieves lower resolution but from larger volumes of biological tissue without sectioning. In addition, the methods also provide complementarity in the obtained information. When comparing PXCT with electron tomography datasets, we observe on the very same sample and similar organelles, differences. Although PXCT and FIB/SEM do display maximum electron density signals on the same features, some other signals of lower intensity did not pinpoint exactly the same features with each method i.e. at the synaptic ends. This property is most probably due to differences between the two methods with respect to the interaction of each beam with matter, and the type of detection. The local elemental contrast obtained with backscattered electrons in FIB/SEM differs with the electron density contrast of PXCT (Diaz et al, 2015; Pfister et al, 2016). For example, at the synapses, the strongest observed intensities were

for both methods located at the ribbon of the synapses, which are rich in proteins, and the hilus of the somatic ribbon synapse. However, while the membranes around cells and organelles were better resolved with the FIB/SEM method because osmium tetroxide interacts with the lipids, PXCT highlighted particularly well and systematically electron-dense structures located e.g. at the junctions of synaptic arciform membranes downstream of the synaptic ribbon (**Fig. S2E-G**). The aforementioned property of hard X-ray tomography should be further exploited with higher resolution and contrast, and in a correlative way. It will likely allow pinpointing supramolecular assemblies, also those barely present in a tissue, according to their density in samples without contrasting agent.

Table1: Comparison of FIB/SEM with PXCT and other X-ray imaging methods:

	FIB/SEM tomography	Hard X-ray nanotomography	Soft X-ray tomography
Principle	backscattered electron detection (Knott et al, 2011)	ptychographic/propagation-based phase contrast hard X-ray tomography (Diaz et al, 2015; Kosior et al, 2012)	soft X-ray (< 2 keV) absorption tomography (Groen et al, 2019)
Spatial resolution	++++	++	+++
sample thickness	+++	+++	++
Sample integrity	slicing	no slicing	no slicing
Sample native contrast	elemental contrast (atomic number z)	electron density	carbon-rich structures vs water

Perspectives of PXCT imaging of the retina and other tissues.

Photoreceptor cells are about 100 µm long and possess usually a long axon travelling until the plexus part to reach the postsynaptic ends of the next neurons layer. Our first attempt to image a retina sample of 25 µm diameter and 20 µm length using hard X-ray ptychographic nanotomography, allowed the analysis of a volume containing 60 nuclei and synaptic connections. We expect that, in the future, improvements in sample preparation (less handling, less staining, with fiducial and correlative options), in the PXCT method and algorithms (Li and Maiden, 2018; Odstrcil et al, 2019; Thibault et al, 2014; Tsai et al, 2016) and in the synchrotron properties (more coherent flux available in next generation synchrotron sources) (Thibault et al, 2014)), will enable imaging of volumes larger than 100 x 100 x 100 µm³ containing hundreds of cells at an isotropic spatial resolution of 50 nm.

MATERIALS AND METHODS:

Fixation, staining and embedding of retina tissue.

C57Bl/6 wild-type and VPP mice were maintained as breeding colonies at the Laboratory Animal Services Center (LASC) of the University of Zurich in a 14 h: 10 h light-dark cycle with lights on at 6 am and lights off at 8 pm. Mice had access to food and water *ad libitum*. All procedures concerning animals were in accordance with the regulations of the Veterinary Authority of Zurich and with the statement of 'The Association for Research in Vision and Ophthalmology' for the use of animals in research.

Enucleated eye globes from wild-type mice or from retinitis pigmentosa mice by 4 weeks of age (RP-mouse) (Naash et al, 1993) were fixed by 2.5% glutaraldehyde in 0.1 M cacodylate buffer pH 7.2 for 12 h at 4°C, trimmed, and the isolated retina was cut through the optic nerve into two parts, superior and inferior. The retina samples were stained 60 min in 1% osmium tetroxide (postfixation) in 0.1 M cacodylate buffer pH 7.2 at room temperature, stepwise dehydrated with increasing ethanol concentrations (15 min each for 30, 50, 70, 90 and 100%), followed by 2 supplementary 15 min-incubation in 100% ethanol and embedded in Epon™ 812 resin (Samardzija et al, 2006a). Microtome sections (Leica Ultracut UCT) of 50 nm analysed by widefield light microscopy (Zeiss Microscope, Axioplan, Jena, Germany) confirmed the quality of the staining, the preservation of the neuronal layers and the cells integrity (**Fig. 1A, left**). The surface selected for further 3D-imaging was coated with a 20 nm gold layer using a Balzers SCD050 sputter coater to make it conductive.

Retina pillar preparation for PXCT

The block of resin-embedded retina was mounted on the stage of a FIB-SEM NVision 40 electron microscope (Zeiss) and the region of interest was localised by SEM (scanning electron microscopy) viewing mode using an SE2 (type 2 secondary electrons) detector and an energy of 2.00 kV (**Fig. 1A, right**). The ONL is the easier layer to recognise because of the highly scattering nuclei. A pillar of around 25 µm diameter and 50µm height was milled (annular milling with 3 nA, then polishing with 700 pA) in the neighbouring outer plexiform layer, OPL (**Fig. 1A, inset**) or in the inner plexiform layer, IPL (not shown) using the focused ion beam (FIB) of the NVision 40 microscope. In this study, the sample was prepared from a region close to the optical nerve and we can therefore assume that the photoreceptor cells are in majority rod cells. The resulting pillar was transferred and welded with carbon, centred on a gold-coated pin for X-ray imaging (Holler et al, 2017a) (**Fig. 1B**) and stored at room temperature. The quality of the pillar could be verified at higher resolution by scanning electron microscopy using an energy selective backscatter (ESB) electron detector and at an energy of 5.00 kV (**Fig. 1B, inset**).

Hard X-ray ptychographic nanotomography at cryogenic temperature.

Pillars of resin-embedded retina from wild-type and RP-model mice were measured using the OMNY instrument (Holler et al, 2012; Holler et al, 2018) operating at the cSAXS beamline of the Swiss Light Source at the Paul Scherrer Institute in Villigen, Switzerland. The OMNY microscope (tOMography Nano crYo) (Holler et al, 2018) provides ideal conditions for 3D imaging with ptychographic hard X-ray computed tomography (PXCT): ultra-high vacuum, cryogenic temperature control and, most importantly, accurate positioning of the sample controlled by laser interferometry (Holler and Raabe, 2015). The samples were mounted on a cryo-stage and were kept in vacuum at a constant temperature of about 90 K during the entire measurements. The measurement details of the wild-type specimen were already reported in an earlier work (Holler et al, 2018) and are copied here for completeness:

"The X-ray photon energy was 6.2 keV and the coherent illumination on the sample was defined by a FZP (Fresnel Zone Plate) made of Au (Gorelick et al, 2011) with 60 nm outer-most zone width. The FZP diameter was 120 μm , the flux of about $2.6 \cdot 10^8$ photons/s, and the specimen was placed at 1.2 mm downstream the focus, such that the illumination on the sample was about 4 μm . The sample was scanned with the high-precision scanner of OMNY at positions following the pattern of a Fermat spiral, as described in Huang et al. (Huang et al, 2014). The field of view covered by the scans was $35 \times 25 \mu\text{m}^2$ (horizontal x vertical) with an average distance between scan positions of about 1.2 μm . Coherent diffraction patterns with 0.1 s exposure time were recorded at each scan position using a Pilatus 2M detector (Henrich et al, 2009; Kraft et al, 2009) placed at 7.335 m downstream the sample. Ptychographic scans were repeated at 333 different angles of the specimen with respect to the incoming beam, spanning a range from 0 to 180 degrees in equal intervals. The total time for acquisition including overhead of motor motions in between acquisitions was about 16.5 h. We estimate that a dose of 1×10^7 Gy was deposited for the measurement."

The RP-model mouse specimen was also measured at a photon energy of 6.2 keV, with the beam also defined by a FZP with 60 nm outer-most zone width. The diameter of the FZP was in this case 220 μm , thereby a coherent photon flux of $4.2 \cdot 10^8$ photons/s was achieved. The sample was placed at 2.4 mm after the FZP, where the size of the beam was about 8 μm . At this position, the specimen was scanned following the pattern of a Fermat spiral over an area of $60 \times 20 \mu\text{m}^2$ (horizontal x vertical) with an average step size of about 2 μm . We used an Eiger 500k detector (Dinapoli et al, 2011) placed 7.314 m downstream to record diffraction patterns at each scanning position with an acquisition time of 0.1 s. Scans were performed at 500 different angular orientations, obtained by rotating the specimen at different angles from 0 to 180 degrees in equal angular intervals. The total acquisition time for this specimen was about 9.7 hours, imparting a dose of about $6.1 \cdot 10^6$ Gy on the specimen.

The diffraction patterns acquired for each ptychographic scan at each angular position were fed into iterative phase retrieval algorithms, more precisely a combination of the difference map (Thibault et al, 2009) and the maximum likelihood algorithms (Thibault and Guizar-Sicairos, 2012) were used. These reconstructions yielded 2D complex-valued images corresponding to each angular projection. The phase of these projections was extracted and corrected for zero and first-order phase terms, which are intrinsic degrees of freedom in ptychographic reconstructions (Guizar-Sicairos et al, 2011), and registered before tomographic reconstruction as described in (Guizar-Sicairos et al, 2011) and (Guizar-Sicairos et al, 2015). The size of the diffraction of patterns used for ptychographic reconstructions was different for each sample: in the case of the wild-type specimen, the diffraction patterns were cropped to 400x400 pixels of

172 μm pixel size, while for the RP-model sample 500 \times 500 pixels of 75 μm pixel size were used. This determined the resulting pixel size in the reconstructed ptychographic projections, which is equal to the voxel size in the tomographic reconstructions, to be 21.9 nm and 39.0 nm for the wild-type and the RP-model specimens, respectively. The spatial resolution of the tomograms was estimated using Fourier shell correlation (FSC). We then computed the FSC between these tomograms, which is a correlation curve between the two 3D datasets in Fourier domain. The resolution was estimated using as threshold the half-bit criterion (van Heel and Schatz, 2005). For this analysis, the 2 independent tomograms where cropped to a 3D region inside the sample containing all cell nuclei, synaptic connections and other structures beyond the synaptic ends which were not well-resolved. The average estimated half-period resolution within such a volume was about 150 nm and 230 nm for the wild-type and for the RP-model samples, respectively. The difference in the two values stems from the lower contrast present in the features of the RP-model sample.

Focused ion beam-scanning electron microscopy (FIB/SEM) (Knott et al, 2011).

The retina pillar from the wild-type mouse analysed using PXCT or the retina in a trimmed Epon™ block (flowchart Fig. S4) were mounted on a regular SEM stub using conductive carbon and coated with 10 nm of carbon by electron beam evaporation to render the sample conductive. Ion milling and image acquisition was performed simultaneously in an Auriga 40 Crossbeam system (Zeiss, Oberkochen, Germany) using the FIBICS Nanopatterning engine (Fibics Inc., Ottawa, Canada). Prior to start the fine milling and imaging, a protective platinum layer of approximately 300 nm was applied on top of the surface of the area of interest overlapping the OPL and ONL of the retina using the single gas injection system at the FIB-SEM. A large trench was milled at a current of 16 nA and 30 kV around the area of interest. For slice & view imaging, a gallium-ion beam of 600 pA at 30 kV and a cutting depth per slice of 20 nm (pillar sample) or 10 nm (OTO sample) was used. The OTO sample ("Osmium- Thiocarbohydrazide-Osmium") (Seligman et al, 1966), consists of a double osmium stain bridged by a reaction with thiocarbohydrazide, and a step of staining with uranyl acetate. The incubation step with uranyl acetate was not conducted in this study. SEM images were acquired at 1.9 kV (60 μm aperture) using an in-lens energy selective backscatter electron detector (ESB) with a grid voltage of 500 V, and a dwell time of 1 μs and a line averaging of 20 lines (OTO sample) or 2 lines (pillar sample). The pixel size was set to 5 nm and was tilt-corrected.

Data Analysis

FIB/SEM tomograms were analysed using the Imaris Image Analysis Software (Bitplane). 3D manual segmentation was performed using the Avizo 3D-Software (FEI). For the PXCT tomograms, the images were binned (2 \times 2 \times 2) and filtered with 2 iterations of anisotropic diffusion (Malik and Perona, 1990) before the manual segmentation.

Supporting information:

- S1: Hard X-ray ptychographic nanotomography (PXCT) of the outer plexus layer of a wild-type mouse retina.
- S2: PXCT imaging of a somatic synapse and image segmentation.
- S3: FIB/SEM imaging of a somatic synapse in the wild-type mouse retina.
- S4: Flowchart of retina nanotomography by PXCT, followed by FIB/SEM.

Movie1: Hard X-ray ptychographic nanotomography (PXCT) of the outer plexus layer of a wild-type mouse retina.

Movie2: PXCT of the outer plexus layer of a retina from a retinitis pigmentosa (RP) mouse disease model.

Movie3: PXCT subtomogram through a somatic synapse from wild-type mouse.

Movie4: FIB/SEM tomogram through of the PXCT-imaged retina pillar of the of the wild-type mouse.

Movie5: FIB/SEM tomogram through a pillar from a stronger osmium-stained wild-type mouse retina.

Acknowledgements: The authors thank Marijana Samardzija (Grimm group, UZH) for discussions and advices on retina degeneration and mice models, and Andrea Gubler (Grimm group, UZH) for excellent technical support. The authors thank Susan Cohrs, Martin Behe and Cristina Müller from the PSI for providing some sacrificed mice that were used in this study.

A part of the sample preparation was done at the Scientific Center for Optical and Electron Microscopy (ScopeM) at the ETH, especially successfully thanks to the initial advices of Roger Wepf (EMEZ; present: UQ/CMM, Australia) and trainings with Philippe Gasser, Falk Lucas and Joakim Reuteler. The authors thank Miriam Lucas (ScopEM), Johannes Ihli (LSB, PSI) and Sousan Abolhassani-Dadras (NES, PSI) for helping with analysing the data using the Avizo software. The electron imaging part was performed with support of the Center for Microscopy and Image Analysis, University of Zurich, with the excellent technical assistance of Moritz Kirschmann. Thanks to Gregor Cicchetti (PSI) for discussions and advices.

Competing interests

The authors declare no competing or financial interests.

Author contributions

V.P., A.D. and G.S. designed the study. A.M. gave initial strategy advises. AG.B. and T.I. gave initial technical advises. C.I and V.P. prepared the retina samples. E.M. and V.P. prepared the retina pillars by FIB/SEM. A.D., M.GS and M.H. conducted the PXCT measurements and tomography reconstructions. A.K. designed, conducted and processed the FIB/SEM imaging. C.G. provided the transgenic retinitis pigmentosa mice and supported the team in manpower and ophthalmology knowledge. V.P. and A.D. analyzed the data and wrote the paper. Funding acquisition: G.S. All authors reviewed the manuscript before submission.

Funding

We thank the Swiss National Science Foundation 31003A_149311 and 31003A_173008 support to C.G. and SNF grant 310030B_173335 to G.S. The development of the OMNY microscope was supported by the SNF R'Equip (Project No. 145056).

REFERENCES:

- Anderson, D. H. and Fisher, S. K.** (1975). Disc shedding in rodlike and conelike photoreceptors of tree squirrels, *Science*, **187**(4180), pp. 953-5. doi: 10.1126/science.187.4180.953
- Behnia, R., Clark, D. A., Carter, A. G., Clandinin, T. R. and Desplan, C.** (2014). Processing properties of ON and OFF pathways for *Drosophila* motion detection, *Nature*, **512**(7515), pp. 427-30. doi: 10.1038/nature13427
- Chen, S., Deng, J., Yuan, Y., Flachenecker, C., Mak, R., Hornberger, B., Jin, Q., Shu, D., Lai, B., Maser, J., Roehrig, C., Paunesku, T., Gleber, S. C., Vine, D. J., Finney, L., VonOsinski, J., Bolbat, M., Spink, I., Chen, Z., Steele, J., Trapp, D., Irwin, J., Feser, M., Snyder, E., Brister, K., Jacobsen, C., Woloschak, G. and Vogt, S.** (2014). The Bionanoprobe: hard X-ray fluorescence nanoprobe with cryogenic capabilities, *J Synchrotron Radiat*, **21**(Pt 1), pp. 66-75. doi: 10.1107/S1600577513029676
- Deng, J., Lo, Y. H., Gallagher-Jones, M., Chen, S., Pryor, A., Jr., Jin, Q., Hong, Y. P., Nashed, Y. S. G., Vogt, S., Miao, J. and Jacobsen, C.** (2018). Correlative 3D x-ray fluorescence and ptychographic tomography of frozen-hydrated green algae, *Sci Adv*, **4**(11), pp. eaau4548. doi: 10.1126/sciadv.aau4548
- Diaz, A., Malkova, B., Holler, M., Guizar-Sicairos, M., Lima, E., Panneels, V., Pigino, G., Bittermann, A. G., Wettstein, L., Tomizaki, T., Bunk, O., Schertler, G., Ishikawa, T., Wepf, R. and Menzel, A.** (2015). Three-dimensional mass density mapping of cellular ultrastructure by ptychographic X-ray nanotomography, *J Struct Biol*, **192**(3), pp. 461-469. doi: 10.1016/j.jsb.2015.10.008
- Dierolf, M., Menzel, A., Thibault, P., Schneider, P., Kewish, C. M., Wepf, R., Bunk, O. and Pfeiffer, F.** (2010). Ptychographic X-ray computed tomography at the nanoscale, *Nature*, **467**(7314), pp. 436-9. doi: 10.1038/nature09419
- Dinapoli, R., Bergamaschi, A., Henrich, B., Horisberger, R., Johnson, I., Mozzanica, A., Schmid, E., Schmitt, B., Schreiber, A., Shi, X. T. and Theidel, G.** (2011). EIGER: Next generation single photon counting detector for X-ray applications, *Nuclear Instruments & Methods in Physics Research Section a-Accelerators Spectrometers Detectors and Associated Equipment*, **650**(1), pp. 79-83. doi: 10.1016/j.nima.2010.12.005
- Ding, X. Q. and Naash, M. I.** (2006). Transgenic animal studies of human retinal disease caused by mutations in peripherin/rds, *Adv Exp Med Biol*, **572**, pp. 141-6. doi: 10.1007/0-387-32442-9_21
- Du, M. and Jacobsen, C.** (2018). Relative merits and limiting factors for x-ray and electron microscopy of thick, hydrated organic materials, *Ultramicroscopy*, **184**(Pt A), pp. 293-309. doi: 10.1016/j.ultramic.2017.10.003
- Foglia, F., Hazael, R., Meersman, F., Wilding, M. C., Sakai, V. G., Rogers, S., Bove, L. E., Koza, M. M., Moulin, M., Haertlein, M., Forsyth, V. T. and McMillan, P. F.** (2019). In Vivo Water Dynamics in *Shewanella oneidensis* Bacteria at High Pressure, *Sci Rep*, **9**(1), pp. 8716. doi: 10.1038/s41598-019-44704-3
- Gorelick, S., Vila-Comamala, J., Guzenko, V. A., Barrett, R., Salome, M. and David, C.** (2011). High-efficiency Fresnel zone plates for hard X-rays by 100 keV e-beam lithography and electroplating, *J Synchrotron Radiat*, **18**(Pt 3), pp. 442-6. doi: 10.1107/S0909049511002366
- Goutman, J. D., Elgoyhen, A. B. and Gomez-Casati, M. E.** (2015). Cochlear hair cells: The sound-sensing machines, *FEBS Lett*, **589**(22), pp. 3354-61. doi: 10.1016/j.febslet.2015.08.030
- Groen, J., Conesa, J. J., Valcarcel, R. and Pereiro, E.** (2019). The cellular landscape by cryo soft X-ray tomography, *Biophys Rev*, pp. 611-619. doi: 10.1007/s12551-019-00567-6
- Guizar-Sicairos, M., Boon, J. J., Mader, K., Diaz, A., Menzel, A. and Bunk, O.** (2015). Quantitative interior x-ray nanotomography by a hybrid imaging technique, *Optica*, **2**(3), pp. 259-266. doi: 10.1364/Optica.2.000259
- Guizar-Sicairos, M., Diaz, A., Holler, M., Lucas, M. S., Menzel, A., Wepf, R. A. and Bunk, O.** (2011). Phase tomography from x-ray coherent diffractive imaging projections, *Opt Express*, **19**(22), pp. 21345-57. doi: 10.1364/OE.19.021345
- Guo, J. and Larabell, C. A.** (2019). Soft X-ray tomography: virtual sculptures from cell cultures, *Curr Opin Struct Biol*, **58**, pp. 324-332. doi: 10.1016/j.sbi.2019.06.012

- Helmstaedter, M., Briggman, K. L., Turaga, S. C., Jain, V., Seung, H. S. and Denk, W.** (2013). Connectomic reconstruction of the inner plexiform layer in the mouse retina, *Nature*, **500**(7461), pp. 168-74. doi: 10.1038/nature12346
- Henrich, B., Bergamaschi, A., Broennimann, C., Dinapoli, R., Eikenberry, E. F., Johnson, I., Kobas, M., Kraft, P., Mozzanica, A. and Schmitt, B.** (2009). PILATUS: A single photon counting pixel detector for X-ray applications, *Nuclear Instruments & Methods in Physics Research Section a-Accelerators Spectrometers Detectors and Associated Equipment*, **607**(1), pp. 247-249. doi: 10.1016/j.nima.2009.03.200
- Heynen, S. R., Meneau, I., Caprara, C., Samardzija, M., Imsand, C., Levine, E. M. and Grimm, C.** (2013). CDC42 is required for tissue lamination and cell survival in the mouse retina, *PLoS One*, **8**(1), pp. e53806. doi: 10.1371/journal.pone.0053806
- Holler, M., Guizar-Sicairos, M., Tsai, E. H., Dinapoli, R., Muller, E., Bunk, O., Raabe, J. and Aepli, G.** (2017a). High-resolution non-destructive three-dimensional imaging of integrated circuits, *Nature*, **543**(7645), pp. 402-406. doi: 10.1038/nature21698
- Holler, M. and Raabe, J.** (2015). Error motion compensating tracking interferometer for the position measurement of objects with rotational degree of freedom, *Optical Engineering*, **54**(5), pp. 054101. doi:
- Holler, M., Raabe, J., Diaz, A., Guizar-Sicairos, M., Quitmann, C., Menzel, A. and Bunk, O.** (2012). An instrument for 3D x-ray nano-imaging, *Rev Sci Instrum*, **83**(7), pp. 073703. doi: 10.1063/1.4737624
- Holler, M., Raabe, J., Diaz, A., Guizar-Sicairos, M., Wepf, R., Odstrcil, M., Shaik, F. R., Panneels, V., Menzel, A., Sarafimov, B., Maag, S., Wang, X., Thominet, V., Walther, H., Lachat, T., Vitins, M. and Bunk, O.** (2018). OMNY-tOMography Nano crYo stage, *Rev Sci Instrum*, **89**(4), pp. 043706. doi: 10.1063/1.5020247
- Holler, M., Raabe, J., Wepf, R., Shahmoradian, S. H., Diaz, A., Sarafimov, B., Lachat, T., Walther, H. and Vitins, M.** (2017b). OMNY PIN-A versatile sample holder for tomographic measurements at room and cryogenic temperatures, *Rev Sci Instrum*, **88**(11), pp. 113701. doi: 10.1063/1.4996092
- Huang, X., Yan, H., Harder, R., Hwu, Y., Robinson, I. K. and Chu, Y. S.** (2014). Optimization of overlap uniformness for ptychography, *Opt Express*, **22**(10), pp. 12634-44. doi: 10.1364/OE.22.012634
- Karreman, M. A., Ruthensteiner, B., Mercier, L., Schieber, N. L., Solecki, G., Winkler, F., Goetz, J. G. and Schwab, Y.** (2017). Find your way with X-Ray: Using microCT to correlate in vivo imaging with 3D electron microscopy, *Methods Cell Biol*, **140**, pp. 277-301. doi: 10.1016/bs.mcb.2017.03.006
- Knott, G., Rosset, S. and Cantoni, M.** (2011). Focussed ion beam milling and scanning electron microscopy of brain tissue, *J Vis Exp*, (53), pp. e2588. doi: 10.3791/2588
- Kosior, E., Bohic, S., Suhonen, H., Ortega, R., Deves, G., Carmona, A., Marchi, F., Guillet, J. F. and Cloetens, P.** (2012). Combined use of hard X-ray phase contrast imaging and X-ray fluorescence microscopy for sub-cellular metal quantification, *J Struct Biol*, **177**(2), pp. 239-47. doi: 10.1016/j.jsb.2011.12.005
- Kraft, P., Bergamaschi, A., Broennimann, C., Dinapoli, R., Eikenberry, E. F., Henrich, B., Johnson, I., Mozzanica, A., Schleputz, C. M., Willmott, P. R. and Schmitt, B.** (2009). Performance of single-photon-counting PILATUS detector modules, *J Synchrotron Radiat*, **16**(Pt 3), pp. 368-75. doi: 10.1107/S0909049509009911
- Krenkel, M., Markus, A., Bartels, M., Dullin, C., Alves, F. and Salditt, T.** (2015). Phase-contrast zoom tomography reveals precise locations of macrophages in mouse lungs, *Sci Rep*, **5**, pp. 9973. doi: 10.1038/srep09973
- Kuan, A. T., Phelps, J. S., Thomas, L. A., Nguyen, T. M., Han, J., Chen, C. L., Azevedo, A. W., Tuthill, J. C., Funke, J., Cloetens, P., Pacureanu, A. and Lee, W. A.** (2020). Dense neuronal reconstruction through X-ray holographic nanotomography, *Nat Neurosci*, **23**(12), pp. 1637-1643. doi: 10.1038/s41593-020-0704-9
- Li, P. and Maiden, A.** (2018). Multi-slice ptychographic tomography, *Sci Rep*, **8**(1), pp. 2049. doi: 10.1038/s41598-018-20530-x
- Li, S., Sukeena, J. M., Simmons, A. B., Hansen, E. J., Nuhn, R. E., Samuels, I. S. and Fuerst, P. G.** (2015). DSCAM promotes refinement in the mouse retina through cell death and restriction of exploring dendrites, *J Neurosci*, **35**(14), pp. 5640-54. doi: 10.1523/JNEUROSCI.2202-14.2015
- Malik, J. and Perona, P.** (1990). Preattentive texture discrimination with early vision mechanisms, *J Opt Soc Am A*, **7**(5), pp. 923-32. doi:
- Massimi, L., Bukreeva, I., Santamaria, G., Fratini, M., Corbelli, A., Brun, F., Fumagalli, S., Maugeri, L., Pacureanu, A., Cloetens, P., Pieroni, N., Fiordaliso, F., Forloni, G., Uccelli, A., Kerlero de Rosbo, N., Balducci, C. and Cedola, A.** (2019). Exploring Alzheimer's disease mouse brain through X-ray phase contrast tomography: From the cell to the organ, *Neuroimage*, **184**, pp. 490-495. doi: 10.1016/j.neuroimage.2018.09.044
- Migdale, K., Herr, S., Klug, K., Ahmad, K., Linberg, K., Sterling, P. and Schein, S.** (2003). Two ribbon synaptic units in rod photoreceptors of macaque, human, and cat, *J Comp Neurol*, **455**(1), pp. 100-12. doi: 10.1002/cne.10501

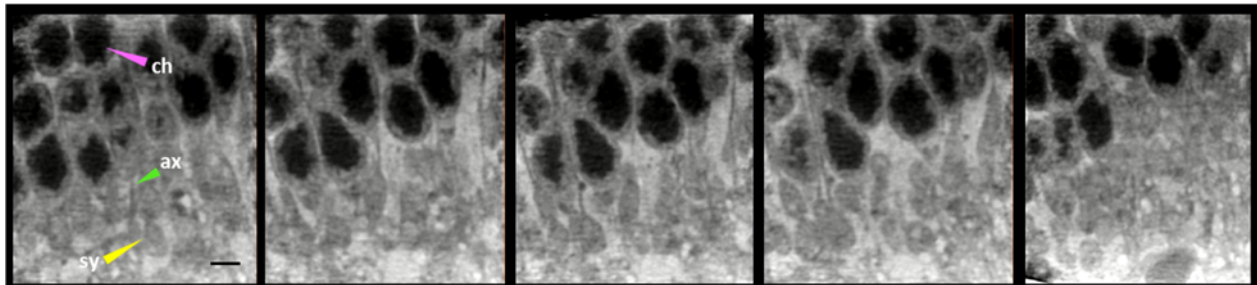
- Naash, M. I., Hollyfield, J. G., al-Ubaidi, M. R. and Baehr, W.** (1993). Simulation of human autosomal dominant retinitis pigmentosa in transgenic mice expressing a mutated murine opsin gene, *Proc Natl Acad Sci U S A*, **90**(12), pp. 5499-503. doi:
- Naash, M. I., Rипps, H., Li, S., Goto, Y. and Peachey, N. S.** (1996). Polygenic disease and retinitis pigmentosa: albinism exacerbates photoreceptor degeneration induced by the expression of a mutant opsin in transgenic mice, *J Neurosci*, **16**(24), pp. 7853-8. doi:
- Odstrcil, M., Lebugle, M., Guizar-Sicairos, M., David, C. and Holler, M.** (2019). Towards optimized illumination for high-resolution ptychography, *Opt Express*, **27**(10), pp. 14981-14997. doi: 10.1364/OE.27.014981
- Pfister, B., Sanchez-Ferrer, A., Diaz, A., Lu, K., Otto, C., Holler, M., Shaik, F. R., Meier, F., Mezzenga, R. and Zeeman, S. C.** (2016). Recreating the synthesis of starch granules in yeast, *eLife*, **5**. doi: 10.7554/eLife.15552
- Prokop, A. and Meinertzhagen, I. A.** (2006). Development and structure of synaptic contacts in Drosophila, *Semin Cell Dev Biol*, **17**(1), pp. 20-30. doi: 10.1016/j.semcd.2005.11.010
- Samardzija, M., Wenzel, A., Aufenberg, S., Thiersch, M., Reme, C. and Grimm, C.** (2006a). Differential role of Jak-STAT signaling in retinal degenerations, *FASEB J*, **20**(13), pp. 2411-3. doi: 10.1096/fj.06-5895fje
- Samardzija, M., Wenzel, A., Naash, M., Reme, C. E. and Grimm, C.** (2006b). Rpe65 as a modifier gene for inherited retinal degeneration, *Eur J Neurosci*, **23**(4), pp. 1028-34. doi: 10.1111/j.1460-9568.2006.04639.x
- Seligman, A. M., Wasserkrug, H. L. and Hanker, J. S.** (1966). A new staining method (OTO) for enhancing contrast of lipid--containing membranes and droplets in osmium tetroxide--fixed tissue with osmiophilic thiocarbohydrazide(TCH), *J Cell Biol*, **30**(2), pp. 424-32. doi:
- Shahmoradian, S. H., Tsai, E. H. R., Diaz, A., Guizar-Sicairos, M., Raabe, J., Spycher, L., Britschgi, M., Ruf, A., Stahlberg, H. and Holler, M.** (2017). Three-Dimensional Imaging of Biological Tissue by Cryo X-Ray Ptychography, *Sci Rep*, **7**(1), pp. 6291. doi: 10.1038/s41598-017-05587-4
- Thibault, P., Dierolf, M., Bunk, O., Menzel, A. and Pfeiffer, F.** (2009). Probe retrieval in ptychographic coherent diffractive imaging, *Ultramicroscopy*, **109**(4), pp. 338-343. doi: 10.1016/j.ultramic.2008.12.011
- Thibault, P. and Guizar-Sicairos, M.** (2012). Maximum-likelihood refinement for coherent diffractive imaging, *New Journal of Physics*, **14**. doi: Artn 063004
10.1088/1367-2630/14/6/063004
- Thibault, P., Guizar-Sicairos, M. and Menzel, A.** (2014). Coherent imaging at the diffraction limit, *J Synchrotron Radiat*, **21**(Pt 5), pp. 1011-8. doi: 10.1107/S1600577514015343
- Topperwien, M., van der Meer, F., Stadelmann, C. and Salditt, T.** (2018). Three-dimensional virtual histology of human cerebellum by X-ray phase-contrast tomography, *Proc Natl Acad Sci U S A*, **115**(27), pp. 6940-6945. doi: 10.1073/pnas.1801678115
- Tran, H. T., Tsai, E. H. R., Lewis, A. J., Moors, T., Bol, J., Rostami, I., Diaz, A., Jonker, A. J., Guizar-Sicairos, M., Raabe, J., Stahlberg, H., van de Berg, W. D. J., Holler, M. and Shahmoradian, S. H.** (2020). Alterations in Sub-Axonal Architecture Between Normal Aging and Parkinson's Diseased Human Brains Using Label-Free Cryogenic X-ray Nanotomography, *Front Neurosci*, **14**, pp. 570019. doi: 10.3389/fnins.2020.570019
- Tsai, E. H., Usov, I., Diaz, A., Menzel, A. and Guizar-Sicairos, M.** (2016). X-ray ptychography with extended depth of field, *Opt Express*, **24**(25), pp. 29089-29108. doi: 10.1364/OE.24.029089
- van Heel, M. and Schatz, M.** (2005). Fourier shell correlation threshold criteria, *Journal of Structural Biology*, **151**(3), pp. 250-262. doi: 10.1016/j.jsb.2005.05.009
- Walker, S. M., Schwyn, D. A., Mokso, R., Wicklein, M., Muller, T., Doube, M., Stampanoni, M., Krapp, H. G. and Taylor, G. K.** (2014). In vivo time-resolved microtomography reveals the mechanics of the blowfly flight motor, *PLoS Biol*, **12**(3), pp. e1001823. doi: 10.1371/journal.pbio.1001823
- Wassle, H.** (2004). Parallel processing in the mammalian retina, *Nat Rev Neurosci*, **5**(10), pp. 747-57. doi: 10.1038/nrn1497
- Wernet, M. F. and Desplan, C.** (2014). Homothorax and Extradenticle alter the transcription factor network in Drosophila ommatidia at the dorsal rim of the retina, *Development*, **141**(4), pp. 918-28. doi: 10.1242/dev.103127
- Wichmann, C. and Moser, T.** (2015). Relating structure and function of inner hair cell ribbon synapses, *Cell Tissue Res*, **361**(1), pp. 95-114. doi: 10.1007/s00441-014-2102-7
- Yonehara, K., Fiscella, M., Drinnenberg, A., Esposti, F., Trenholm, S., Krol, J., Franke, F., Scherf, B. G., Kusnyerik, A., Muller, J., Szabo, A., Juttner, J., Cordoba, F., Reddy, A. P., Nemeth, J., Nagy, Z. Z., Munier, F., Hierlemann, A. and Roska, B.** (2016). Congenital Nystagmus Gene FRMD7 Is Necessary for Establishing a Neuronal Circuit Asymmetry for Direction Selectivity, *Neuron*, **89**(1), pp. 177-93. doi: 10.1016/j.neuron.2015.11.032

Supplemental Data

Imaging of retina cellular and subcellular structures using ptychographic hard X-ray tomography.

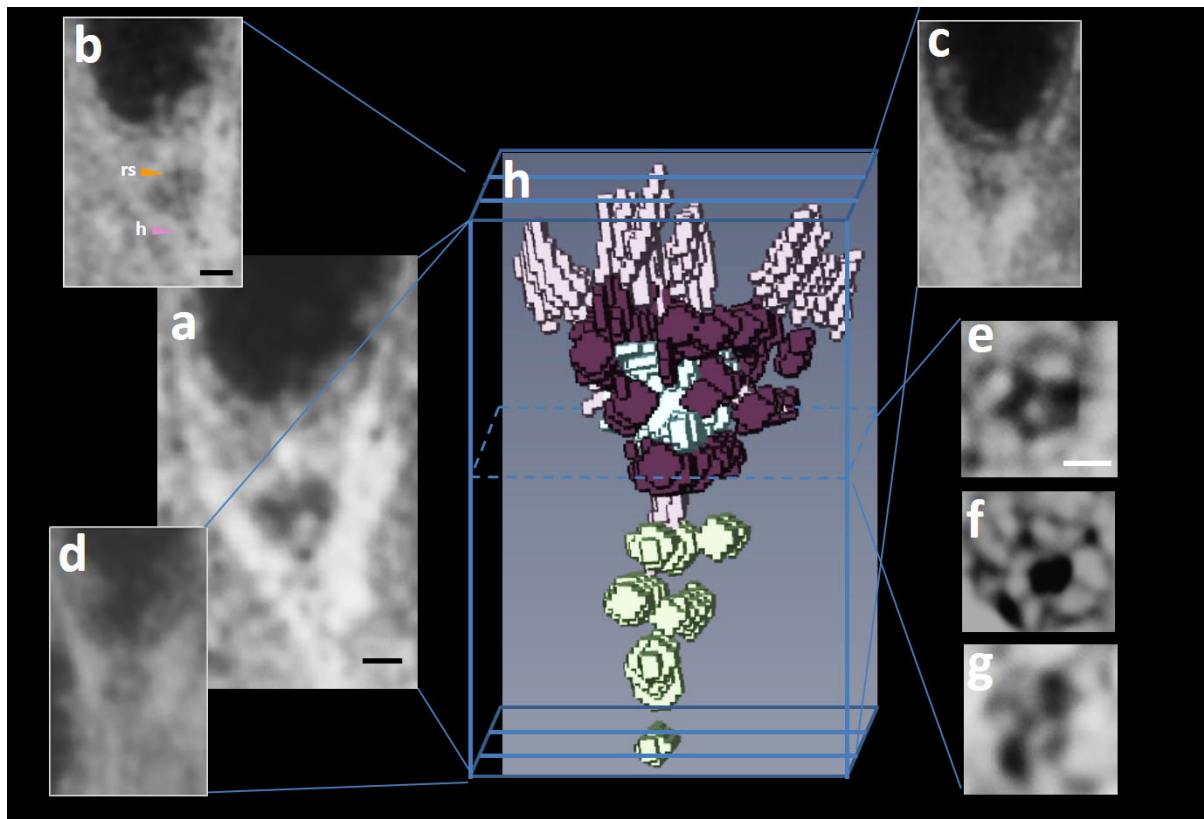
Panneels V., Diaz A., Imsand C., Guizar Sicairos M., Müller E., Bittermann AG., Ishikawa T., Menzel A., Kaech A., Holler M., Grimm C. and Schertler G.

Fig. S1: Hard X-ray ptychographic nanotomography (PXCT) of the outer plexus layer (25 μm diameter-micropillar of 20 μm height) of a wild-type mouse retina.



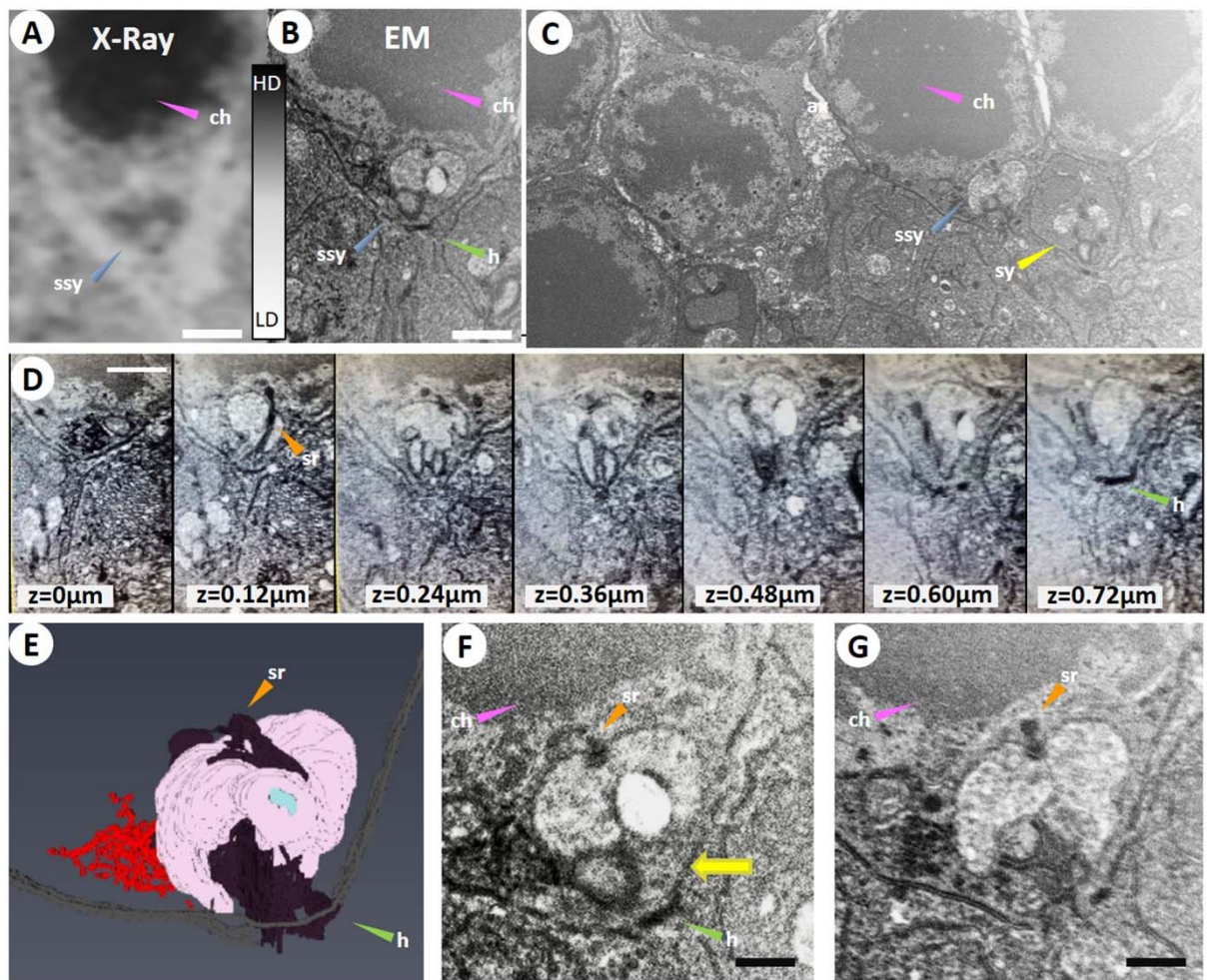
Representative consecutive orthoslices (*yz directions*) through a region of interest of the reconstructed tomogram. Chromatin "ch" (magenta arrows) from the nucleus located in the outer nuclei layer (ONL); axonal projections "ax" (green arrows) and synaptical terminal end "sy" (yellow arrows) from the outer plexiform layer (OPL). Scale bar: 3 μm .

Fig. S2: PXCT imaging of a somatic synapse and image segmentation.



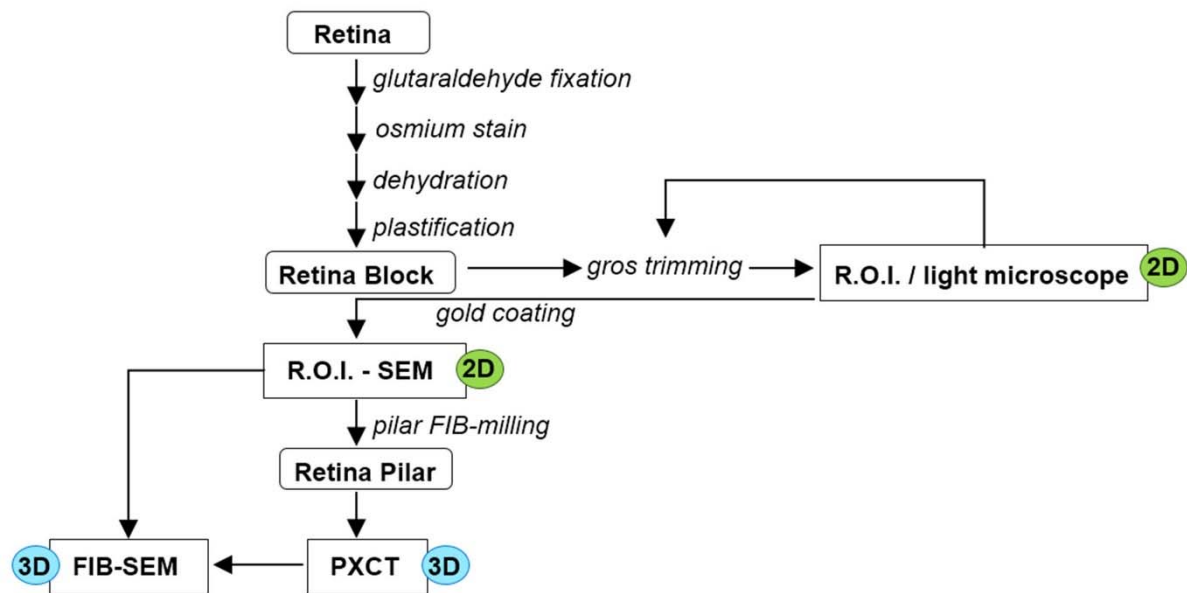
Orthoslices of one neuron of the wild-type retina, found in the PXCT tomogram, that shows a synapse in the soma. **a-d.** are views in the longitudinal X,Y and Y,Z directions ("rs" is the ribbon synapse, "h" points the hilus) and **e-g.** in the transversal X,Z direction. Black is high density and white lower density. Black and white scale bars are 1 μ m and 500 nm, respectively. **h.** A manual segmentation of the subcellular structures was done with the Avizo™ software. The ribbon and active zones are in brown, a vacuole of low electron density in light blue, some structures connecting the synapse to the nucleus are in dark pink and some postsynaptic features are colored in green.

Fig. S3: FIB/SEM imaging of a somatic synapse in the wild-type mouse retina.

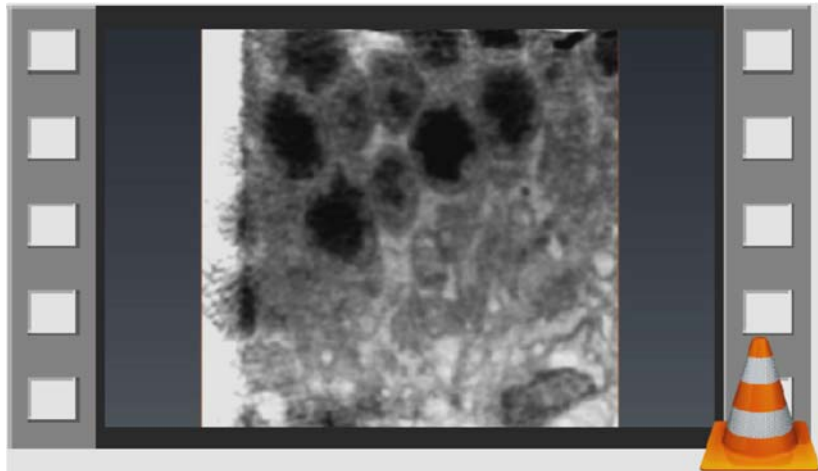


(A-B): Orthoslices of the retina tomograms, comparing a somatic synapse imaged by PXCT (A) and by FIB/SEM ("EM") out of the X-rayed pillar (B). The grayscales show the distribution range from high (HD) to low (LD) electron density. Scale bar is 1 μm. Legend of subcellular structures: nuclei packed with dense chromatin ("ch", magenta arrows), synaptical termini ("sy", yellow arrows), somatic synapse ("ssy", blue arrows), synaptic ribbon ("sr", orange arrows), hilus ("h", green arrows). **(C)** FIB/SEM overview of the region of interest (field of view 14 μm x 7 μm) at the interface between the ONL and OPL retina layers from the OTO-epoxy block. **(D)** Consecutive FIB/SEM orthoslices through a somatic synapse. The synaptic ribbon (orange) and the hilus (green) give a very strong signal, and, in general, the membrane structures are well resolved. **(E)** Manual segmentation of the structure. The ribbon, active zones and hilus are in brown, the vacuole of low electron density is in light blue, the pre- / postsynaptic membranes are in pink and some synaptic vesicles are in red. **(F-G)** Two different views of the somatic synapse showing the structure of the electron dense arciform synaptic membranes (G) and vesicles trapped inside (F, yellow arrow). Scale bar of G: 500 nm.

Fig. S4: Flowchart of retina nanotomography by PXCT, followed by FIB/SEM.



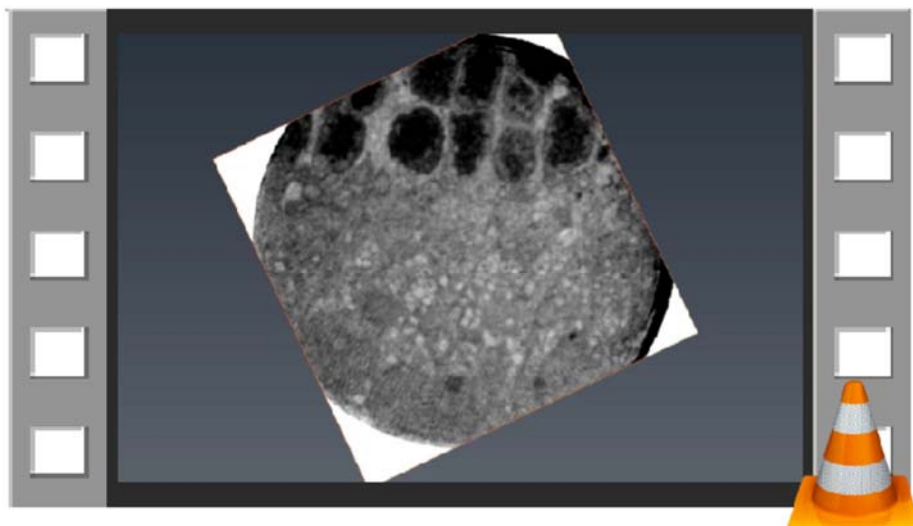
Movie 1: Hard X-ray ptychographic nanotomography (PXCT) of the outer plexus layer (25 μm diameter-micropillar of 20 μm height) of a wild-type mouse retina



file: movie1.mp4

Reconstructed tomogram (voxel size 44nm, field of view $\sim 20 \times 20 \mu\text{m}^2$) from wild-type mouse retina.

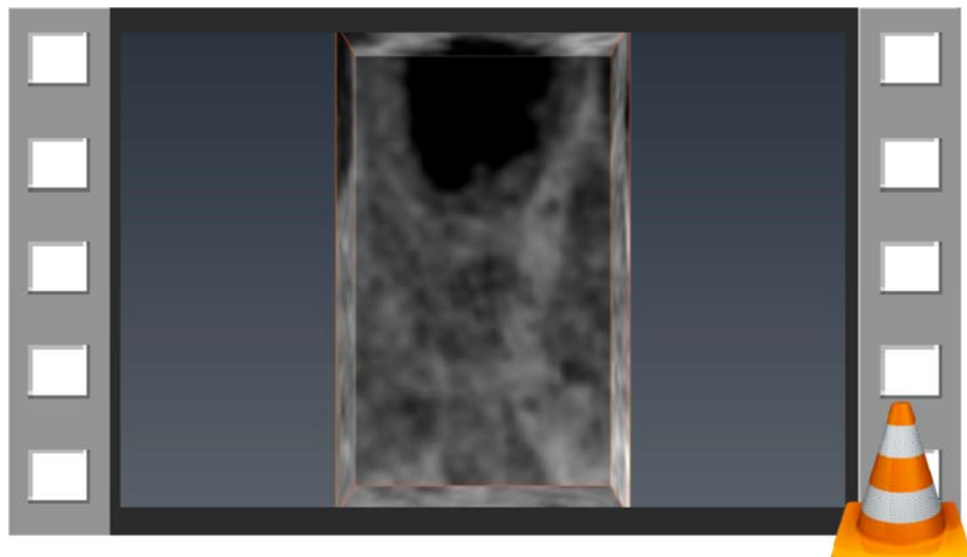
Movie 2: PXCT of the outer plexus layer of a retina from a retinitis pigmentosa (RP) mouse disease model.



file: movie2.mp4

Reconstructed tomogram (voxel size 44nm, field of view $\sim 20 \times 20 \mu\text{m}^2$) from the degenerative retina of VPP-mouse, model of retinitis pigmentosa.

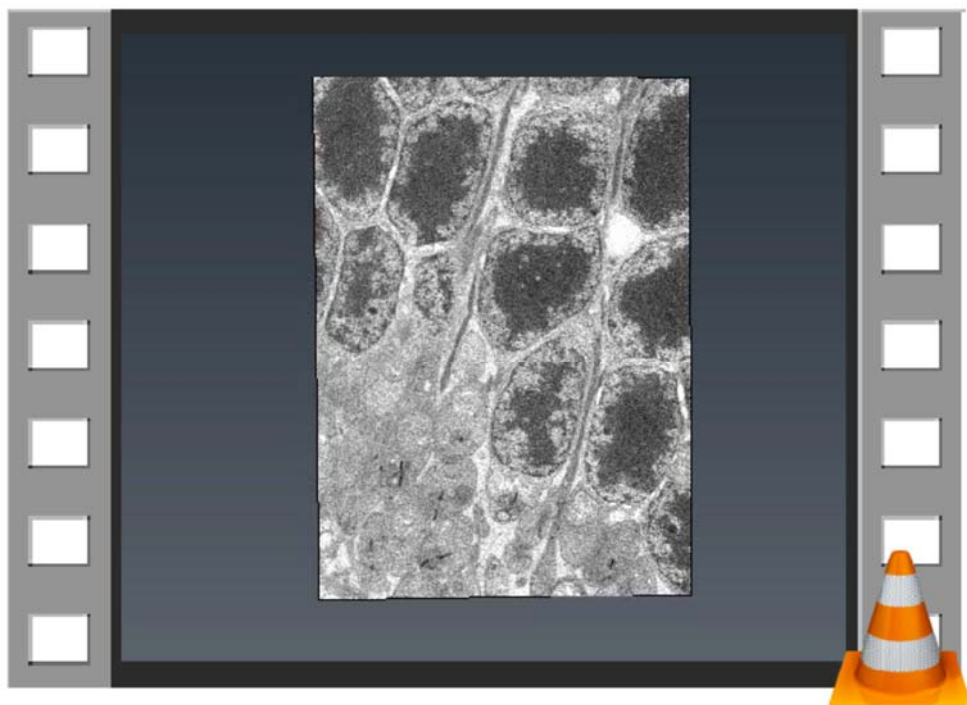
Movie 3: PXCT subtomogram through a somatic synapse from wild-type mouse.



file: movie3.mp4

Subvolume of the tomogram from wild-type retina with field of view $4 \times 6.5 \mu\text{m}^2$.

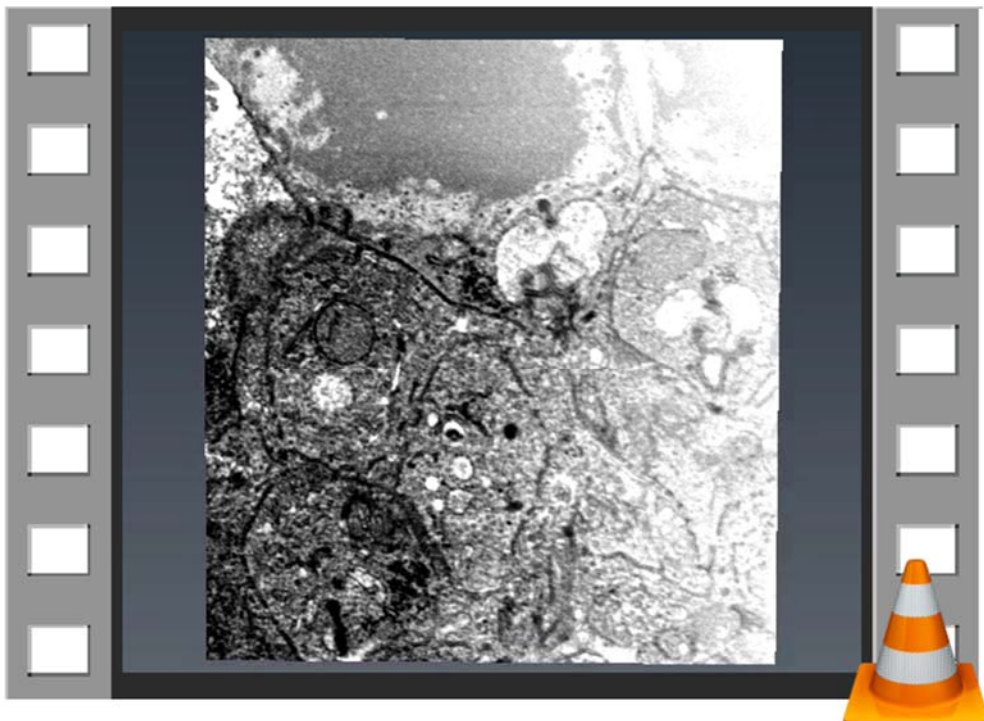
Movie 4: FIB/SEM tomogram through the PXCT-imaged retina pillar of the wild-type mouse.



file: movie4.mp4

Reconstructed tomogram from the X-ray measured pillar from wild-type mouse retina imaged by FIB/SEM. Movie created from 109 orthoslices displayed at 25 frames per second, field of view $12 \times 16 \mu\text{m}^2$

Movie5: FIB/SEM tomogram through a pillar from a stronger osmium-stained wild-type mouse retina (OTO-stained retina).



file: movie5.mp4

Reconstructed tomogram from wild-type mouse retina imaged by FIB/SEM displayed at 25 frames per second, field of view $7 \times 8 \mu\text{m}^2$.